Bridging-nitrogen defects modified graphitic carbon nitride nanosheet for boosted photocatalytic hydrogen production

Lei Luo[a], Keran Wang[a], Zhuyu Gong[a], Haixing Zhu[a], Jiani Ma[a]*, Lunqiao Xiong[b], Junwang Tang[b]*

[a] Key Lab of Synthetic and Natural Functional Molecule Chemistry of Ministry of Education, the Energy and Catalysis Hub, College of Chemistry and Materials Science, Northwest University, Xi'an, P. R. China.

[b] Department of Chemical Engineering, University College London, Torrington Place, London WC1E 7JE, UK.

Abstract

Reinforcing the visible photon absorption and charge separation are the key issues to maximize the photocatalytic performance of graphitic carbon nitride. Herein, holey bridging-nitrogen-defected graphitic carbon nitride nanosheets were prepared through solid-state copolymerization and subsequently thermal annealing with melamine and hexamethylenetetramine as the precursors. Numerous pores and bridging nitrogen defects that embedded into the thin-layer framework were evidenced through comprehensive characterization. The synthesized textural and electronic structure enables the significant improvement of photocatalytic hydrogen production, with the optimized sample of D-CNNS(0.3) representing a hydrogen evolution rate of 2497.1 $\mu mol \cdot g^{-1} \cdot h^{-1}$ under visible light irradiation ($\lambda > 420$ nm). This is about 10.4 and 41.1 folds improvement compared with pristine nanosheets and bulk carbon nitride, respectively. Both experimental and theoretical results demonstrate the bridging nitrogen defects are beneficial to enhance photoabsorption, promote charge separation and transfer. Together with the enlarged surface area, the optimized nanosheet sample shows a dramatically improved quantum yield in visible region.

Keywords: *Solar hydrogen, spatial charge separation, photoabsorption, N-defects doped graphitic carbon nitride, surface engineering.*

1. Introduction

Photocatalysis is an environmentally friendly approach and can be applied to many energy intensive processes, including water splitting, carbon dioxide photoreduction, direct methane conversion and contaminant decomposition [1-8]. The key to promote the practical application of solar conversion is the development of an efficient visible-light responsive photocatalyst [9-12]. Among various photocatalysts, graphitic carbon nitride (CN) was recently emerged as a remarkable candidate for its easily regulated properties and narrow bandgap energy (2.7 eV) [13, 14]. However, pristine CN demonstrates moderate reactivity because of its low surface area (ca. 10 m^2/g), severe electron-hole recombination and weak visible-light absorption[15]. To achieve improved photoreactivity, diverse strategies were explored, for instance, morphological engineering [16-19], doping [20-23], defect modification [24-26] and heterojunction construction [27-32]. In spite of extensive and attractive researches, highly efficient, earth-abundant and low-cost photocatalysts are still rare.

Two-dimensional CN nanosheets prevail mainly because of an enhanced specific surface area and short diffusion distance from the internal to the surface. Through thermal or liquid exfoliation via disrupting the interlayer Van der Waals' force, CN nanosheets were prepared and exhibited enhanced photocatalysis [33, 34]. However, nanoscaled CN still suffers from a detrimental drawback of enlarged bandgap owing to the quantum confinement effect, leading to the decreased efficiency in utilizing visible light. Surface modification through bandgap engineering could insert doping energy level among the bandgap, thus modifying the electronic structure and enhancing photoabsorption [35]. The method for defect modification of g-C_3N_4 can be divided as the top-down and bottom-up methods. In the former, thermal annealing in various atmosphere [36-40] or at rapid ramping temperature [41, 42] could introduce defects and realize the molecular-level modification of the polymeric structure.

Meanwhile, thermal-treatment with additives, such as ammonium thiosulfate [43] and NaBH$_4$ [44, 45] could also produce nitrogen-defected g-C$_3$N$_4$. As a contrast, the bottom-up method was realized through controlling the polymerization temperature [46], or polymerizing with additives including N$_2$H$_4$·H$_2$O [47], NH$_4$Cl [24], NH$_4$NO$_3$ [48] and KOH [49]. With these success, there are still a few areas to be improved in order to obtain a more efficient and economical photocatalysts, such as reducing the use of solvent and oxygenated agent, simplifying the multi-step procedure, or increasing relatively low surface area. Moreover, the defects might serve as the deep trapping sites for photogenerated charge carrier and hinder its further reaction with the surface electron acceptors [50, 51]. In this regard, to combine the features of nanosheets and defects, it is highly attractive to rationally regulate the moderate defect sites on CN nanosheets via reliable strategy.

Our previous work shows that the band structure and positions of CN are very sensitive to the bridging nitrogen. In this work, bridging nitrogen defects modified holey CN nanosheets were thus prepared via solid-state copolymerization followed by the successively thermal annealing for realizing defects introduction and structural exfoliation. The holey and bridging defect structure were evidenced by HRTEM, XPS and ^{13}C NMR. Holey nanosheet structure would provide more accessible active sites and shorten charge transfer distance. And the experimental and theoretical results synchronously confirmed the enhanced photoabsorption, enlarged surface area and charge separation induced by the bridging-nitrogen defects, which eventually boosting the visible-light photocatalytic water splitting for hydrogen evolution. The optimized hydrogen evolution rate of the as-prepared CN reaches 2495.1 μmol·g^{-1}·h^{-1} in visible region, about 10.4 and 41.1 folds improvements than that of pristine bulk and nanosheet CN, with its apparent quantum yield reaching 3.24% at 420 ± 10 nm.

2. Experimental

2.1. Materials

All chemicals were reagent grade and used without any purification. Melamine, triethanolamine (TEOA), hexamethylenetetramine (HMTA), chloroplatinic acid ($H_2PtCl_6·6H_2O$) were used.

2.2. Preparation of the bridging nitrogen defects modified CN

Bulk carbon-rich CN (C-BCN(x)) were synthesized from the copolymerization of HMTA and melamine in muffle under the static air atmosphere. Totally, a certain amount of HMTA and 10.0 g melamine were mixed and uniformly grounded in an agate mortar for about 10 minutes. The mixtures were then placed in a 100 mL crucible with a lid and underwent calcination at 550 °C for 3 h with a ramping rate of 10 °C/min. The as-obtained grey materials were finely grounded for further utilization and donated as C-BCN(x), where x represented the mass percent (wt.%) of HMTA.

Bridging nitrogen defects modified holey CN nanosheets (denoted as D-CNNS(x)) were further prepared through thermal annealing C-BCN(x) in air. Typically, 0.5 g C-BCN(x) were dispersed in the crucible and calcinated at 500 °C for 4 h, and the light grey powders were obtained after naturally cooling down. For comparison, pristine bulk and nanosheet CN were prepared under the same conditions except without HMTA, coded as BCN and CNNS, respectively. In the following discussion, C-BCN and D-CNNS refer to C-BCN(0.3) and D-CNNS(0.3) otherwise specified.

2.3. Characterization

Elemental analysis (EA) were obtained on the *VarioEL III* elemental analyzer. High-resolution transmission electron microscope (HRTEM) images were collected on the *Talos F200X* instrument. Nitrogen physical adsorption-desorption isotherms were measured at -196 °C on the *TR2 Star3020* gas adsorption analyzer. All samples were degassed before measurement at 150 °C for 8 h and backfilled with ultrapure nitrogen (99.999%). Powder X-Ray diffraction patterns (XRD) were collected on the *D8 ADVANCE* diffractometer (*Bruker Co., Ltd*). Fourier transform-infrared (FT-IR)

spectra were measured on the *TENSOR27* instrument. X-ray photoelectric spectra (XPS) were conducted on the *PHI 5000 VersaProbeIII* instrument (*ULVAC-PHI Co., Ltd*). UV-Vis diffuse reflectance spectra (DRS) were obtained with $BaSO_4$ as the references on the *UV-3600 Plus* spectrophotometer (*Shimadzu Co., Ltd*). Steady-state photoluminescence (PL) spectra were recorded at room temperature with a 310 nm excitation wavelength. Time-resolved PL spectra were collected on the *FLSP920* spectrofluorometer.

2.4. Photocatalytic hydrogen production

Photocatalytic H_2 production from water spitting was conducted in a 500 mL finely closed quartz reactor. The light source was provided by a 300 W Xe lamp (*PLS-SXE300D, Beijing Perfectlight Technology Co., Ltd*) equipped with the optical filter ($\lambda > 420$ nm). In a typical experiment, 50 mg photocatalysts were mixed with 180.0 g distilled water, 22.4 g TEOA and certain amount of H_2PtCl_6 (3.0 wt.% Pt) solution. Before irradiation, the suspension was stirred and purged with ultrapure argon (99.999 vol.%) for 1 h. Hydrogen was detected with 1 h intervals by the gas *3240A* chromatograph (*Beifen Ruili Co., Ltd*) equipped with the 5 Å molecular sieve column and thermal conductivity detector (TCD). The apparent quantum yield (AQY) was measured and calculated by the followed equation.

$$AQY\ (\%) = \frac{2 \times \text{amount of } H_2 \text{ molecules evolved}}{\text{number of incident photons}}$$

2.5. Electrochemical measurements

The electrochemical properties including electrochemical impedance spectroscopy (EIS), Mott-schottky plots and photocurrent density were measured with the three-electrode cell on the CHI660E workstation. Ag/AgCl electrode, photocatalysts coated indium tin oxide (ITO) glass, platinum sheet

electrode and Na$_2$SO$_4$ solution (0.1 M) were respectively utilized as the reference electrode, the working electrode, the counter electrode and the electrolyte. The working electrode was prepared through electroplating according to our previous work [17]. Photocurrent density was recorded by using a 420 nm LED lamp as the light source.

3. Results and discussion

Bridging-nitrogen defects modified CN nanosheets were prepared through carbon incorporation and subsequently selective elimination. As illustrated in **Figure 1a**, the graphitic carbon and CN composites (GC/CN) firstly formed after bottom-up copolymerization. The uniform inserted graphitic carbon clusters would then be eliminated and generate numerous mesopores. More importantly, the matrix would exfoliate to nanosheets during thermal annealing, then resulting in the holey nanosheet structure. Meanwhile, the electronic configuration might be synchronously regulated. As shown in **Figure S1**, the carbonization of HMTA causes a well-controlled and proportional improvement of C to N ratio. As the usage of HMTA rising, the C/N ratio of C-BCN(x) gradually improves from 0.677 of C-BCN(0.1) to 0.691 of C-BCN(1.0), being attributed to the increased content of graphitic carbon species. After thermal annealing of BCN in air to form sample of CNNS, its C/N ratio slightly decreases, mainly due to the enlarged surface area which derived much more uncondensed amino groups. In the case of D-CNNS(x), the C/N ratio presents regular decrease primarily due to the graphitic carbon elimination. However, samples D-CNNS(x) still remains the higher and regular C/N ratio than that of the pristine CNNS, thus demonstrating the existence of additional carbon atoms or decreased nitrogen atoms along with CN.

The structural features were investigated with the high-resolution transmission electron microscopy (HRTEM). It is clear that BCN performs the dense and thick morphology (**Figure S2**).

As a contrast, CNNS consists of the curly nanosheets (**Figure 1b, c**), suggesting the transformation from thick aggregates to apparent nanosheets with the aid of thermal exfoliation. For C-BCN, a similar dense structure is observed but probably embedded with uniformly distributed graphitic carbon clusters derived from the HMTA carbonization. After thermal annealing, the as-obtained D-CNNS still contains amorphous and exfoliated nanosheets (**Figure 1d, e**) but with numerous mesopores (larger than 20 nm) embedded throughout the networks as circled by the white dash line. This holey nanosheet morphology could be ascribed to the thermally-driven elimination of the graphitic carbon species. Together with the two-dimensional structure, it would provide more active sites, shorten the mass/charge carrier transfer distance and then be beneficial to enhance photocatalysis. The uniform elemental distributions of C and N in D-CNNS are visualized in terms of the TEM-mapping images (**Figure 1f**). Atomic force microscope (AFM) together with the according height profile was conducted to measure the actual thickness of CNNS and D-CNNS. As shown in **Figure 1g-h**, ultrathin CNNS with the thickness of ca. 5.2 nm and D-CNNS with the thickness of ca. 3.8 nm are observed. As the interlayer spacing of CN is about 0.36 nm, CNNS and D-CNNS would have 14 and 10 molecule layers in thickness. The slightly smaller thickness of D-CNNS than CNNS would be attributed to carbon dioxide emission from the oxidation of graphitic carbon, promoting the interlayer thermal exfoliation.
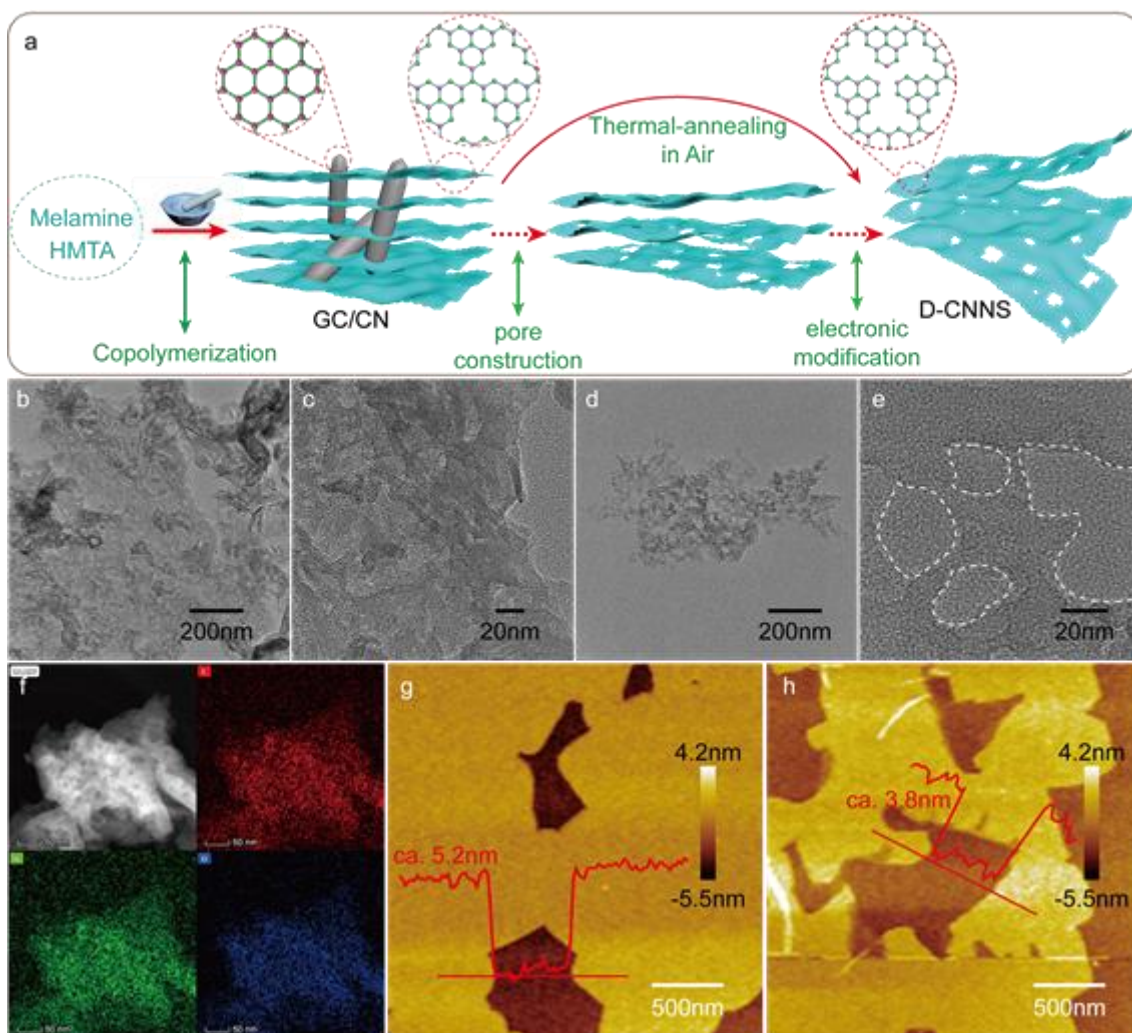
Figure 1. (a) Experimental illustration for the fabrication of the bridging-nitrogen defected holey CN nanosheet (D-CNNS). HRTEM images of (b, c) CNNS and (d, e) D-CNNS. The circled area is the embedded hole. (f) TEM-mapping images of D-CNNS. AFM images of (g) CNNS and (h) D-CNNS.

Nitrogen physical adsorption-desorption isotherms were conducted to study the corresponding changes of the specific surface area along with its thickness. As shown in **Figure 2a**, the representative type-IV adsorption isotherms were present, suggesting the similar layer-stacking topology of BCN, CNNS and D-CNNS. The Brunauer-Emmett-Teller surface area (S_{BET}) of D-CNNS is calculated as 164.7 m^2/g, with 10.6, 11.4 and 1.3-folds increase relative to that of BCN (15.5 m^2/g),

C-BCN (14.4 m^2/g) and CNNS (122.9 m^2/g), corresponding with its thinner layer structure. For BCN

and C-BCN, no mesopores or macropores were observed in **Figure S3**. After thermal annealing,

mesopores and macropores larger than 2 nm were generated into the obtained CNNS and D-CNNS,

correspondingly their pore volume was improved from 0.04 cm^3/g of BCN to 0.49 cm^3/g of CNNS
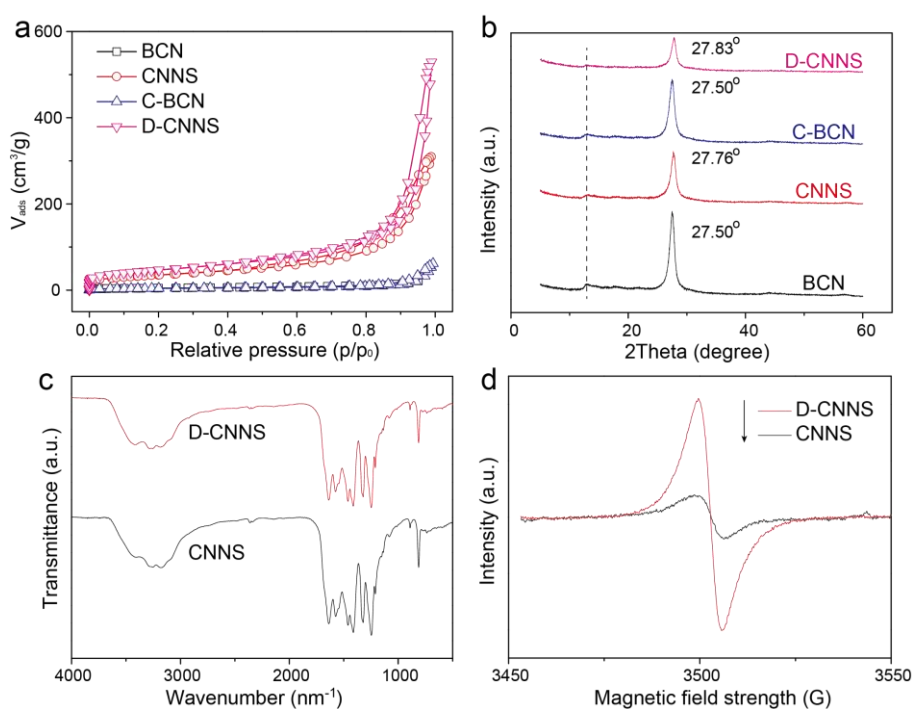
and 0.83 cm^3/g of D-CNNS.

Figure 2. (a) Nitrogen physical adsorption-desorption isotherms at 77 K and (b) XRD patterns of

BCN, CNNS, C-BCN and D-CNNS. (c) FT-IR and (d) EPR spectra of CNNS and D-CNNS.

X-ray diffraction (XRD) patterns were conducted and the results were shown in **Figure 2b**. Two

diffraction peaks at 12.95° and 27.50° in the pristine bulk CN (BCN) are assigned to the in-plane

repeating motifs of continuous heptazine and the periodic stacking of π-conjugated layers,

respectively. This confirms the formation of the typical amorphous graphitic carbon nitride

framework. As a comparison, the dominant (002) peak of CNNS exhibits right-shifted to 27.76°,

indicating its narrower interlayer distance than that of BCN according to the Bragg's law ($2dsin\theta=n\lambda$). It could be attributed to the higher polymerization degree originated from the secondary polymerization derived from the thermal annealing. The narrowed interlayer distance might be beneficial to the vertical charge transfer [52]. Meanwhile, when defining the relative polymerization degree (RPD) of BCN as 100%, CNNS performs the decreased RPD at 64%, assigned to the thermal exfoliation effect [33]. In the case of C-BCN, the (002) peak exhibits the same position at 27.50° but obviously decreased RPD to 74% of BCN. After thermal annealing, the as-obtained D-CNNS shows an obviously right-shifted and decreased peak at 27.83° to 39% RPD. The further right-shifted peak demonstrates the deep polymerization which might be caused by the graphitic carbon oxidation that companied by the local exothermic heat, while the decreased RPD suggests the much thinner thickness.

Fourier transform-infrared (FT-IR) spectra (**Figure 2c**) exhibit similar and typical short-range composition of graphitic carbon nitride. The sharp absorption band at 810 cm^{-1} and series bands ranging from 1200 to 1650 cm^{-1} represent the bending vibration and the stretching vibration of heptazine heterocycles. The broad band around 3000~3500 cm^{-1} is assigned to O-H or N-H, originated from the adsorbed moisture or the uncondensed amino groups [53]. As the absorption band at 2177 cm^{-1} is attributed to the asymmetric stretching vibration of cyano group (C≡N) and generally comes from the breakage of heptazine heterocycles [44, 54], the absence of this peak evidences the well-reserved characteristic heptazine framework. Therefore, the above mentioned high carbon to nitrogen ratio, as evidenced by elemental analysis, would likely be due to N defects on the bridging sites.

The electron paramagnetic resonance (EPR) signals of CN originates from its π-conjugated structure with considerable unpaired electron [55]. As shown in **Figure 2d**, both CNNS and D-CNNS exhibit single Lorentzian lines. Compared with CNNS, D-CNNS presents a much stronger EPR

intensity, suggesting its higher delocalization of the conjugated networks, which might be attributed to the introduction of the bridging sp^3-C atoms or the partial elimination of bridging nitrogen atoms. The improved concentration of free electrons would increase carrier density and be beneficial to photocatalysis.
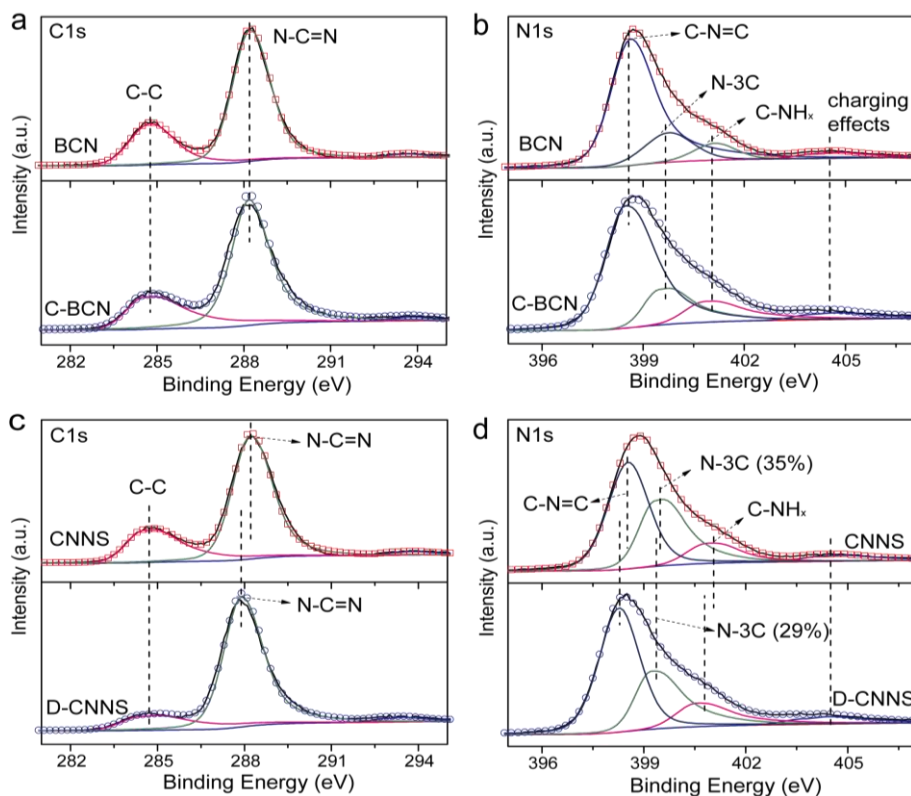

Figure 3. (a) C1s and (b) N1s XPS spectra of BCN and C-BCN. (c) C1s and (d) N1s XPS spectra of CNNS and D-CNNS.

X-ray photoelectron spectra (XPS) were measured to investigate the chemical state of the tailored CN. XPS survey spectra (**Figure S4**) shows the similar elemental composition of carbon, nitrogen and oxygen, where the oxygen element probably comes from the adsorbed moisture [48]. High resolution C1s spectra (**Figure 3a**) of BCN represent two peaks at 284.8 and 288.2 eV, corresponding with the adventitious carbon (C-C/C=C) and sp^2 hybridized carbon in the heptazine heterocycles,

respectively. Compared with BCN, C-BCN exhibits the same binding energy but with an increased C=C content from 26.0% of BCN to 27.3% of C-BCN, attributed to the additional composition of graphitic carbon. Comparing high resolution C1s spectra of BCN, C-BCN and CNNS (**Figure 3a, c**), one can see the same and typical characteristics of CN. While a close look at **Figure 3c**, the peak arising from N-C=N shifts from 288.2 eV of CNNS to 287.9 eV of D-CNNS, suggesting the corresponding carbon atom in the heterocycles exhibits higher electron density in the latter. Combination with the well-reserved heterocycle structure by FT-IR, the higher electron density of carbon in N-C=N would evidence the existence of the carbon replacement or nitrogen vacancy on the bridging-nitrogen sites. Furthermore, N1s peak of C-N=C in D-CNNS (**Figure 3d**) exhibits 0.2 eV shift to lower binding energy and the N-3C contents decrease from 35% of CNNS to 29% of D-CNNS, indicating the loss of partial bridging nitrogen atoms. Therefore, we could presumably conclude the two possible structure including the carbon substitution and nitrogen elimination on the bridging sp^3-N sites. The finely structure were further investigated by the solid ^{13}C nuclear magnetic resonance (NMR) spectra. As shown in **Figure 4a**, only two dominant peaks at chemical shifts of 165.4 and 157.5 ppm were observed and could be attributed to the C-NH$_x$ and N-C=N, respectively. The area ratio of these two peaks declines from 1.87 of pristine CNNS to 1.75 of D-CNNS, which is assigned to the loss of amino groups, corresponding with the XPS analysis. As the carbon bridging structure would show a peak at 136.4 ppm (C=C), the absence of this peak for D-CNNS clearly evidences the bridging-nitrogen defected topology. Therefore, together with the above elemental analysis, we could conclude that the bridging sp^3 N sites were partially removed to generate N vacancies or N defects during the secondary thermal annealing step.
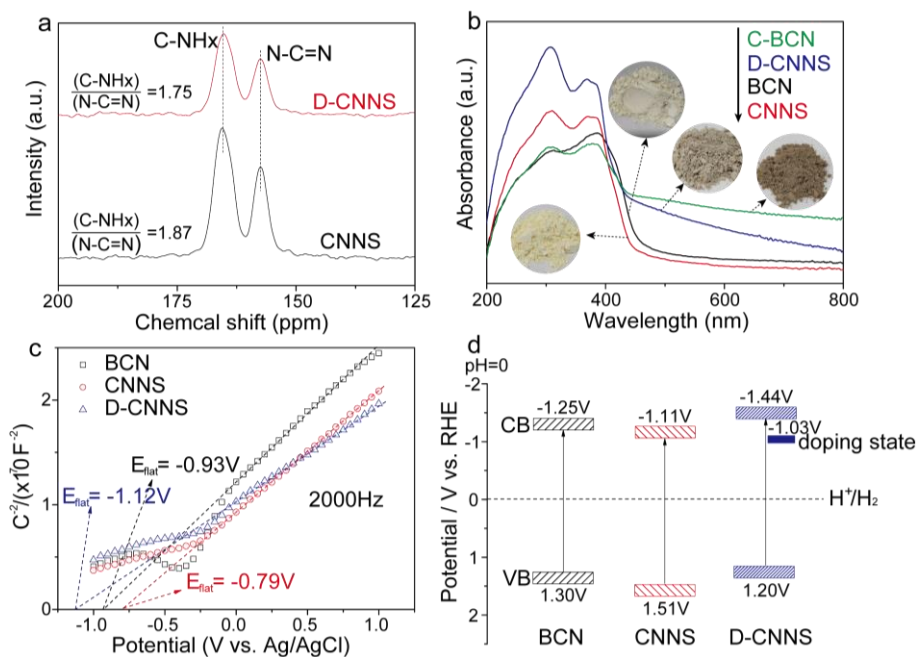
Figure 4. (a) ^{13}C NMR, (b) UV-DRS spectra, (c) Mott-Schottky plots at the selected frequencies of 2000 Hz and (d) bandgap structure of different photocatalysts. The inset of b shows the optical images of BCN, CNNS, C-BCN and D-CNNS.

UV diffuse reflectance spectra (UV-DRS) (**Figure 4b and Figure S5**) were conducted to study the optical properties. Compared with BCN, a blue-shift of the photoabsorption edge for pristine CNNS is observed, due to the quantum confinement effect [56]. Meanwhile, both C-BCN and D-CNNS exhibit an extended light-harvesting ranging from UV to visible region. For C-BCN which served as the intermediate to prepare D-CNNS, the enhanced visible light absorption is assigned to the graphitic carbon. As D-CNNS has no graphitic carbon after thermal annealing in air, the enhanced visible light absorption could be ascribed to the enhanced n → π* optical transition, which is induced by the bridging-nitrogen defects. Tauc plots were used to determine the bandgap energy (**Figure S5**). The bandgap energy of BCN and CNNS are respectively 2.55 eV and 2.62 eV, while D-CNNS presents two bandgap energy at 2.64 eV and 2.23 eV. The latter is the doping state that comes from the nitrogen vacancies. **Figure 4c** exhibits the Mott-Schottky plots of BCN, CNNS and D-CNNS. The positive

slope indicates the n-type semiconductor characteristic of the samples. As the flat band potential of n-type semiconductor lies 0.1 eV below conduction band (CB) [57, 58], the corresponding CB were established as -1.03 eV of BCN, -0.89 eV of CNNS and -1.22 eV of D-CNNS vs Ag/AgCl (pH = 7), respectively. The band positions with respect to RHE (pH = 0) are provided in **Figure 4d**, clearly presenting the energetically feasible to drive the photocatalytic hydrogen production reaction.
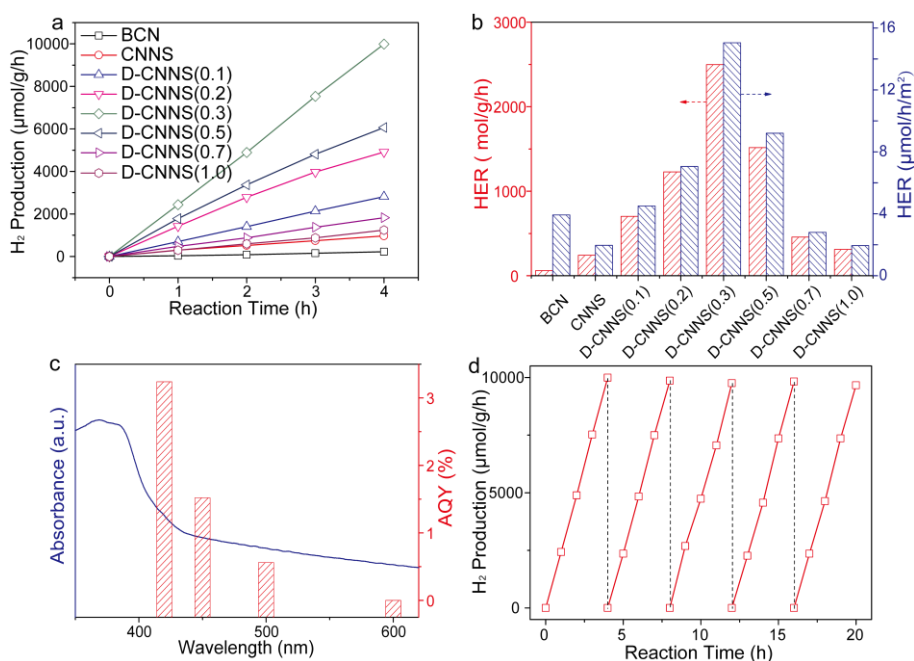

Figure 5. (a) Comparison of the photocatalytic hydrogen evolution rate on different photocatalysts (λ > 420 nm). (b) Hydrogen evolution rates against mass and surface area. (c) Apparent quantum yield versus wavelength and (d) reusability of D-CNNS.

Photocatalytic activity was evaluated by water splitting reaction for hydrogen production under visible-light irradiation (λ > 420 nm). 3 wt.% Pt and 10 vol.% TEOA were used as the co-catalyst and sacrificial agent, respectively. As shown in **Figure 5a**, pristine BCN exhibits obvious hydrogen evolution activity, demonstrating the enough reduction ability of CN for water splitting. In the presence of the pristine CNNS, the hydrogen evolution rate (HER) increases to 241.2 $\mu mol \cdot g^{-1} \cdot h^{-1}$,

about 4.0 times higher than BCN, mainly attributed to the enlarged surface area, which would provide much more accessible active sites and shorten charge transfer distance from the bulk to the surface, thus reducing charge recombination in the bulk. For the nitrogen-defected samples, HER gradually improves with the doping content rising and reaches highest at 2497.1 $\mu mol \cdot g^{-1} \cdot h^{-1}$ for D-CNNS(0.3), about 10.4 and 41.1 times higher than the pristine CNNS and BCN, respectively. Further increasing the nitrogen defects leads to a decreased HER due to the shielding effect [59]. **Figure 5b** shows HRE per unit mass and per unit surface area. The amount of HER per unit surface area of D-CNNS is 15.2 $\mu mol \cdot h^{-1} \cdot m^{-2}$, still 3.9 and 7.6 times higher than that of BCN (3.9 $\mu mol \cdot h^{-1} \cdot m^{-2}$) and CNNS (2.0 $\mu mol \cdot h^{-1} \cdot m^{-2}$). Therefore, the enlarged surface area of D-CNNS can not interpret the boosted photocatalysis, while the nitrogen defects would contributes more, due to the extended photoabsorption region and promoted charge separation as discussed below. The apparent quantum yield (AQY) at different monochromatic light was measured and consistent with its range of photoabsorption (**Figure 5c**). The AQY of D-CNNS could reach 3.2 % at 420 ± 10 nm and 6.9 % at 365 ± 10 nm. Moreover, the nitrogen defected D-CNNS also exhibit acceptable stability with no obvious deactivation after 5 cycles reuse (**Figure 5d**).
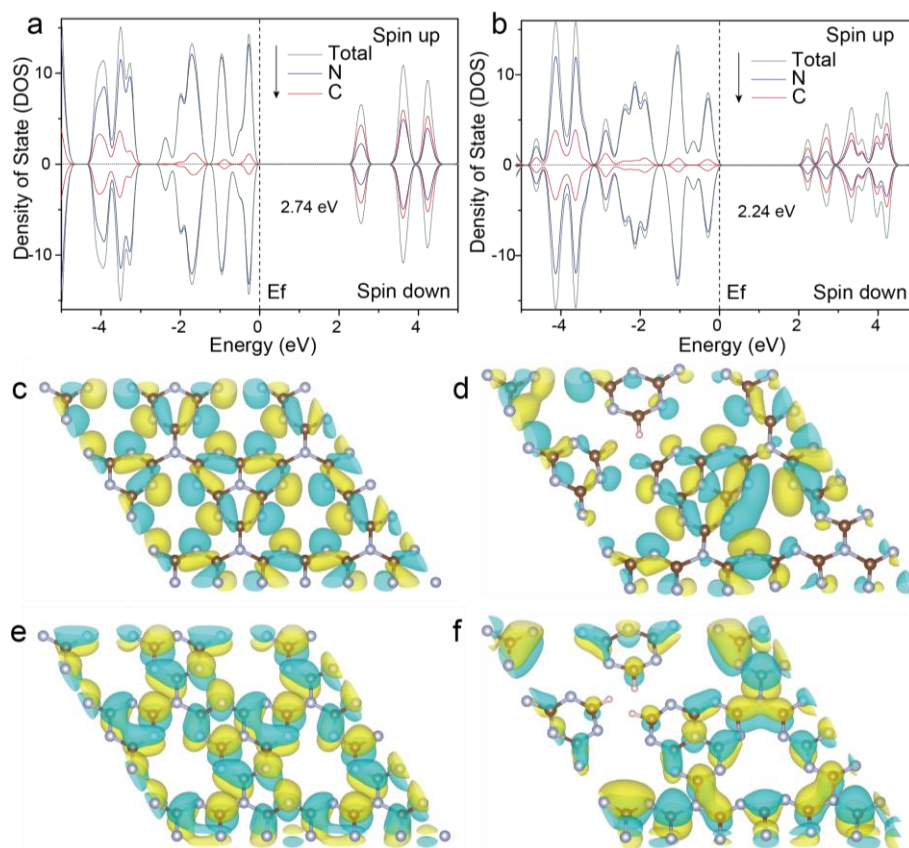
Figure 6. The density of states of (a) C_3N_4 and (b) D-C_3N_4. (c) HOMO and (e) LUMO of pristine C_3N_4. (d) HOMO and (f) LUMO of the bridging-nitrogen defected D-C_3N_4.

Theoretical calculation was performed to understand the enhanced photocatalytic activity. The density of states calculation shows that the pristine CN (C_3N_4) has a large bandgap of 2.74 eV (**Figure 6a**). After eliminating the partial bridging nitrogen atoms and saturating with hydrogens (D-C_3N_4) (**Figure 6b**), the bandgap greatly decreases to 2.24 eV, which is consistent with the enhanced visible-light absorption. From the HOMO/LUMO diagram (**Figure 6c-f**), most atoms before and after nitrogen defects modification contribute to the energy level, which also provides a large number of active sites in the photocatalytic reaction. Compared with the pristine CN, the introduced bridging nitrogen defects change the initial distribution of the energy level planes, which would provide the possibility for electron excitation transitions and spatial charge separation.

Efficient charge separation was experimentally evidenced by the steady-state photoluminescence (PL) spectra and photocurrent response curves. As shown in **Figure 7a**, BCN exhibits a strong PL emission peak, indicating the fast charge recombination, which was considered as one of the main factors that suppresses photocatalysis. For CNNS, the PL intensity greatly decreases, representing suppressed charge recombination, due to the shortened charge transfer path from the internal to the surface. In the case of D-CNNS, the further decreased PL intensity is ascribed to the bridging-nitrogen defects promoting the spatial charge separation. Photocurrent response (**Figure 7b**) also demonstrates the improved charge separation efficiency of D-CNNS. The photocurrent of D-CNNS was measured as 0.18 $\mu A/cm^2$, almost 2 and 4 times higher than that of CNNS and BCN. Besides the enhanced charge separation, the prolonged charge carrier lifetime is also beneficial to the photocatalysis and evidenced by the time-resolved PL spectra (**Figure 7c**). Compared with BCN, both the average lifetime of CNNS (0.48 ns) and D-CNNS (0.61 ns) are longer than that of BCN (0.45 ns). The prolonged lifetime is attributed to the synergy of holey nanosheet texture and defected electronic structure. The nanosheet structure could favor shorter charge transfer distance and the bridging-nitrogen defects would performs as the shallow trapping sites to promote charge separation. [51] Electrochemical impedance spectroscopy (EIS) Nyquist plot (**Figure 7d**) clearly presents the smallest radius of D-CNNS than that of BCN and CNNS. This decreased arc radius indicates a smaller resistance of D-CNNS, which is beneficial to the interfacial charge transfer.
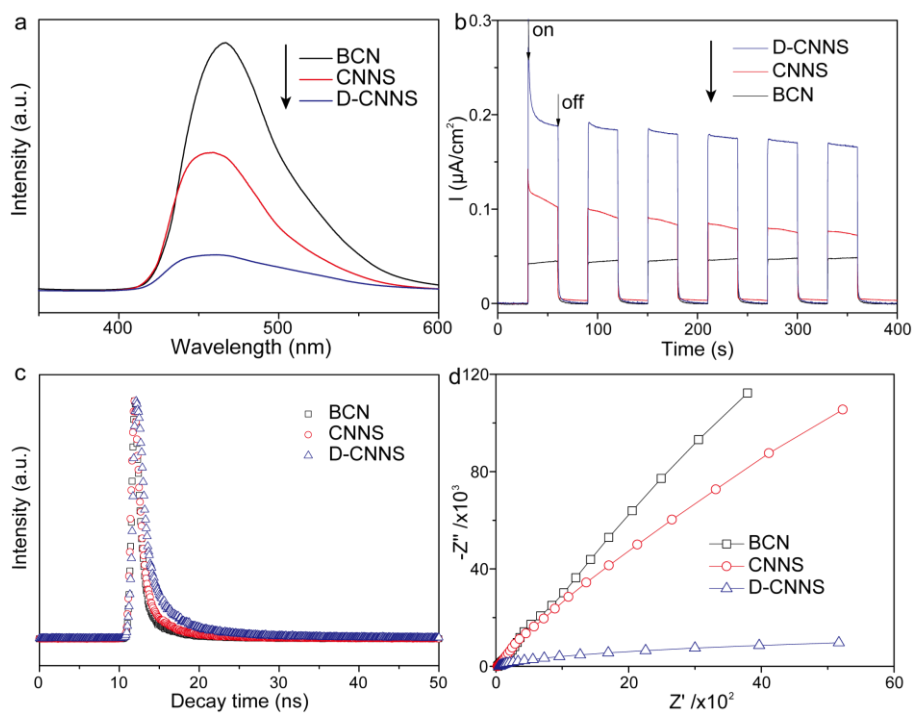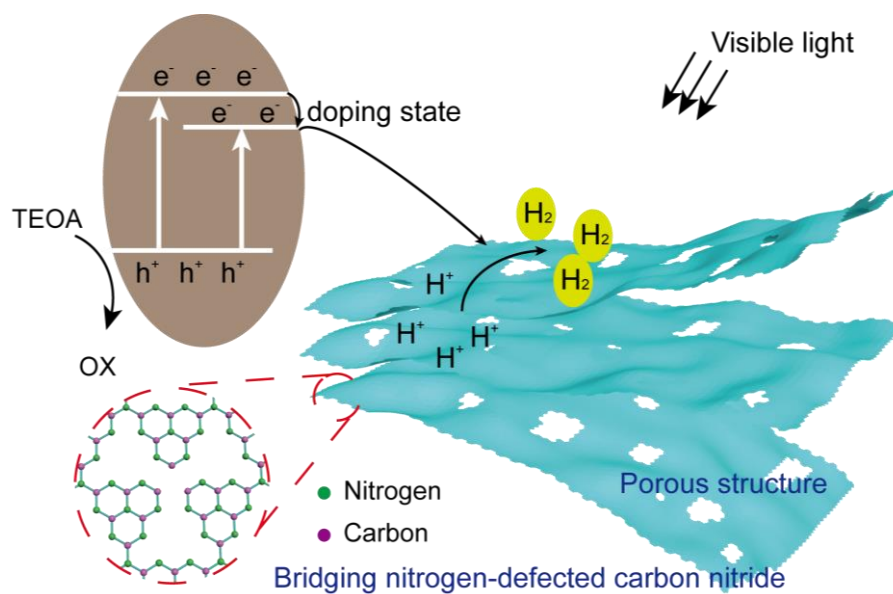
Figure 7. (a) Steady-state PL spectra, (b) photocurrent responses versus time, (c) time-resolved PL

decay spectra and (d) EIS plots of BCN, CNNS and D-CNNS.

Scheme 1. Photocatalytic hydrogen production mechanism on the bridging-nitrogen defects doped

holey CN nanosheets.

The origin of the excellent visible light photocatalytic activity of the tailored CN is proposed as

Scheme 1. The holey nanosheet structure with enlarged surface area is one of the main factors that affects photocatalysis through providing more accessible active sites and shorten charge transfer distance from the bulk to the surface of a photocatalyst, thus reducing charge recombination in the bulk. Consequently, pristine CNNS present 4 times higher HER against mass. However, the enlarged S_{BET} could also affect photoabsorption under the quantum confinement effect, which caused only about 50% HER against S_{BET} for CNNS as that of BCN. D-CNNS exhibits large surface area ($S_{BET} =$ 164.7 m^2/g) associated with the construction of pores structure along the ultra-thin nanolayer (ca. 3.8 nm), which is beneficial to the maximized exposure of active sites to H$^+$. Meanwhile, the bridging-nitrogen defects help to form the doping state and narrow the bandgap as evidenced by the UV-DRS and DOS calculations. The narrowed bandgap enables D-CNNS to greatly expand the range of photoabsorption. Moreover, spatial charge separation is also greatly enhanced as demonstrated by theoretical calculation and time resolved PL spectra. As a result, photocatalytic performance is boosted owing to the synergy of large surface area, morphological and electronic modification via facile solid-state polymerization and successively thermal annealing.

4. Conclusions

In summary, novel bridging-nitrogen defects modified holey graphitic carbon nitride nanosheets (D-CNNS) were prepared via solid-state polymerization and successively thermal annealing with melamine and HMTA as the precursors, in which both porous structure and bridging-nitrogen defects are embedded into the nanosheet framework. It renders the significantly improvement of photocatalytic hydrogen production (2497.1 μmol·g^{-1}·h^{-1}) under visible light irradiation, with the AQY reaches 3.24% at 420 nm ± 10 nm. The holey nanosheet structure with enlarged surface area would provide more accessible active sites and shorten charge transfer distance from the bulk to the

surface. Experimental and theoretical results support that the bridging nitrogen defects would greatly enhance photoabsorption and reduce charge recombination in the bulk apart from the enlarged surface area. This present work provides a simple, low-cost and effective way to simultaneously regulate the textural and electronic structure for improved solar energy utilization.

Conflicts of interest

There are no conflicts to declare.

Acknowledgements

References

[1] L. Grunenberg, G. Savasci, M.W. Terban, V. Duppel, I. Moudrakovski, M. Etter, R.E. Dinnebier, C. Ochsenfeld, B.V. Lotsch, Amine-Linked Covalent Organic Frameworks as a Platform for Postsynthetic Structure Interconversion and Pore-Wall Modification, J. Am. Chem. Soc., 143 (2021) 3430-3438.

[2] Y. Wang, A. Vogel, M. Sachs, R.S. Sprick, L. Wilbraham, S.J.A. Moniz, R. Godin, M.A. Zwijnenburg, J.R. Durrant, A.I. Cooper, J. Tang, Current understanding and challenges of solar-driven hydrogen generation using polymeric photocatalysts, Nature Energy, 4 (2019) 746.

[3] J.-S.M. Lee, A.I. Cooper, Advances in Conjugated Microporous Polymers, Chem. Rev., 120 (2020) 2171-2214.

[4] J. Xie, R. Jin, A. Li, Y. Bi, Q. Ruan, Y. Deng, Y. Zhang, S. Yao, G. Sankar, D. Ma, J. Tang, Highly selective oxidation of methane to methanol at ambient conditions by titanium dioxide-supported iron species, Nat. Catal., 1 (2018) 889.

[5] A. Kumar, A. Kumar, V. Krishnan, Perovskite Oxide Based Materials for Energy and

Environment-Oriented Photocatalysis, ACS Catal., 10 (2020) 10253-10315.

[6] I. Ghosh, J. Khamrai, A. Savateev, N. Shlapakov, M. Antonietti, B. König, Organic semiconductor photocatalyst can bifunctionalize arenes and heteroarenes, Science, 365 (2019) 360.

[7] S. Ghosh, A. Nakada, M.A. Springer, T. Kawaguchi, K. Suzuki, H. Kaji, I. Baburin, A. Kuc, T. Heine, H. Suzuki, R. Abe, S. Seki, Identification of Prime Factors to Maximize the Photocatalytic Hydrogen Evolution of Covalent Organic Frameworks, J. Am. Chem. Soc., 142 (2020) 9752-9762.

[8] K.L. Corp, C.W. Schlenker, Ultrafast Spectroscopy Reveals Electron-Transfer Cascade That Improves Hydrogen Evolution with Carbon Nitride Photocatalysts, J. Am. Chem. Soc., 139 (2017) 7904-7912.

[9] Z. Wang, C. Li, K. Domen, Recent developments in heterogeneous photocatalysts for solar-driven overall water splitting, Chem. Soc. Rev., 48 (2019) 2109.

[10] A. Kumar, V. Navakoteswara Rao, A. Kumar, A. Mushtaq, L. Sharma, A. Halder, S.K. Pal, M.V. Shankar, V. Krishnan, Three-Dimensional Carbonaceous Aerogels Embedded with Rh-SrTiO3 for Enhanced Hydrogen Evolution Triggered by Efficient Charge Transfer and Light Absorption, ACS Applied Energy Materials, 3 (2020) 12134-12147.

[11] M. Melchionna, P. Fornasiero, Updates on the Roadmap for Photocatalysis, ACS Catal., 10 (2020) 5493-5501.

[12] Q. Wang, K. Domen, Particulate Photocatalysts for Light-Driven Water Splitting: Mechanisms, Challenges, and Design Strategies, Chem. Rev., 120 (2020) 919-985.

[13] W.J. Ong, L.-L. Tan, Y.H. Ng, S.-T. Yong, S.-P. Chai, Graphitic Carbon Nitride (g-C$_3$N$_4$)-Based Photocatalysts for Artificial Photosynthesis and Environmental Remediation: Are We a Step Closer To Achieving Sustainability?, Chem. Rev., 116 (2016) 7159.

[14] M.A. Mohamed, M.F. M. Zain, L.J. Minggu, M.B. Kassim, J. Jaafar, N.A. Saidina Amin, Z.A. Mohd Hir, M.S. Rosmi, Enhancement of visible light photocatalytic hydrogen evolution by bio-mimetic C-doped graphitic carbon nitride, Int. J. Hydrogen Energy, 44 (2019) 13098-13105.

[15] A.J. Rieth, Y. Qin, B.C.M. Martindale, D.G. Nocera, Long-Lived Triplet Excited State in a Heterogeneous Modified Carbon Nitride Photocatalyst, J. Am. Chem. Soc., 143 (2021) 4646-4652.

[16] H. Niu, W. Zhao, H. Lv, Y. Yang, Y. Cai, Accurate design of hollow/tubular porous g-C$_3$N$_4$ from melamine-cyanuric acid supramolecular prepared with mechanochemical method, Chem. Eng. J., 411 (2021) 128400.

[17] L. Luo, J. Ma, H. Zhu, J. Tang, Embedded carbon in the carbon nitride hollow sphere for enhanced charge separation and photocatalytic water splitting, Nanoscale, 12 (2020) 7339.

[18] L. Luo, K. Li, A. Zhang, H. Shi, G. Zhang, J. Ma, W. Zhang, J. Tang, C. Song, X. Guo, Controllable assembly of single/double-thin-shell g-C$_3$N$_4$ vesicles via a shape-selective solid-state templating method for efficient photocatalysis, J. Mater. Chem. A, 7 (2019) 17815.

[19] N. Yandrapalli, T. Robinson, M. Antonietti, B. Kumru, Graphitic Carbon Nitride Stabilizers Meet Microfluidics: From Stable Emulsions to Photoinduced Synthesis of Hollow Polymer Spheres, Small, 16 (2020) 2001180.

[20] Y. Li, S. Wang, W. Chang, L. Zhang, Z. Wu, R. Jin, Y. Xing, Co-monomer engineering optimized electron delocalization system in carbon-bridging modified g-C$_3$N$_4$ nanosheets with efficient visible-light photocatalytic performance, Appl. Catal. B-Environ., 274 (2020) 119116.

[21] L. Luo, Z. Gong, J. Ma, K. Wang, H. Zhu, K. Li, L. Xiong, X. Guo, J. Tang, Ultrathin sulfur-doped holey carbon nitride nanosheets with superior photocatalytic hydrogen production from water, Appl. Catal. B-Environ., (2021) 119742.

[22] H. Gao, R. Cao, S. Zhang, H. Yang, X. Xu, 3D hierarchical g-C$_3$N$_4$ architectures assembled by ultrathin self-doped nanosheets: extremely facile HMTA activation and superior photocatalytic hydrogen evolution, ACS Appl. Mater. Inter., 11 (2018) 2050.

[23] J. Jiang, S. Cao, C. Hu, C. Chen, A comparison study of alkali metal-doped g-C3N4 for visible-light photocatalytic hydrogen evolution, Chin. J. Catal., 38 (2017) 1981-1989.

[24] D. Zhang, Y. Guo, Z. Zhao, Porous defect-modified graphitic carbon nitride via a facile one-step approach with significantly enhanced photocatalytic hydrogen evolution under visible light irradiation, Appl. Catal. B-Environ., 226 (2018) 1.

[25] H. Yu, R. Shi, Y. Zhao, T. Bian, Y. Zhao, C. Zhou, G.I.N. Waterhouse, L.-Z. Wu, C.-H. Tung, T. Zhang, Alkali-Assisted Synthesis of Nitrogen Deficient Graphitic Carbon Nitride with Tunable Band Structures for Efficient Visible-Light-Driven Hydrogen Evolution, Adv. Mater., 29 (2017) 1605148.

[26] V.W.-h. Lau, V.W.-z. Yu, F. Ehrat, T. Botari, I. Moudrakovski, T. Simon, V. Duppel, E. Medina, J.K. Stolarczyk, J. Feldmann, V. Blum, B.V. Lotsch, Urea-Modified Carbon Nitrides: Enhancing Photocatalytic Hydrogen Evolution by Rational Defect Engineering, Adv. Energy Mater., 7 (2017) 1602251.

[27] Q. Xu, L. Zhang, B. Cheng, J. Fan, J. Yu, S-Scheme Heterojunction Photocatalyst, Chem, 6

(2020) 1543.

[28] W.-K. Jo, N.C.S. Selvam, Z-scheme CdS/g-C$_3$N$_4$ composites with RGO as an electron mediator for efficient photocatalytic H$_2$ production and pollutant degradation, Chem. Eng. J., 317 (2017) 913-924.

[29] N. Raeisi-Kheirabadi, A. Nezamzadeh-Ejhieh, A Z-scheme g-C3N4/Ag3PO4 nanocomposite: Its photocatalytic activity and capability for water splitting, Int. J. Hydrogen Energy, 45 (2020) 33381-33395.

[30] H. Sepahvand, S. Sharifnia, Photocatalytic overall water splitting by Z-scheme g-C3N4/BiFeO3 heterojunction, Int. J. Hydrogen Energy, 44 (2019) 23658-23668.

[31] A. Kumar, P. Raizada, P. Singh, R.V. Saini, A.K. Saini, A. Hosseini-Bandegharaei, Perspective and status of polymeric graphitic carbon nitride based Z-scheme photocatalytic systems for sustainable photocatalytic water purification, Chem. Eng. J., 391 (2020) 123496.

[32] U. Caudillo-Flores, F. Ansari, B. Bachiller-Baeza, G. Colón, M. Fernández-García, A. Kubacka, (NH4)4[NiMo6O24H6].5H2O / g-C3N4 materials for selective photo-oxidation of CO and CC bonds, Appl. Catal. B-Environ., 278 (2020) 119299.

[33] P. Niu, L. Zhang, G. Liu, H.-M. Cheng, Graphene-Like Carbon Nitride Nanosheets for Improved Photocatalytic Activities, Adv. Funct. Mater., 22 (2012) 4763.

[34] A. Bafekry, B. Akgenc, S.F. Shayesteh, B. Mortazavi, Tunable electronic and magnetic properties of graphene/carbon-nitride van der Waals heterostructures, Appl. Surf. Sci., 505 (2020) 144450.

[35] Y. Li, C. Barløse, J. Jørgensen, B.D. Carlsen, K.A. Jørgensen, Cover Picture: Asymmetric Catalytic Aza-Diels–Alder/Ring-Closing Cascade Reaction Forming Bicyclic Azaheterocycles by Trienamine Catalysis, Chemistry – A European Journal, 23 (2017) 1.

[36] P. Niu, L.C. Yin, Y.Q. Yang, G. Liu, H.M. Cheng, Increasing the visible light absorption of graphitic carbon nitride (melon) photocatalysts by homogeneous self-modification with nitrogen vacancies, Adv. Mater., 26 (2014) 8046.

[37] Q. Liang, Z. Li, Z.-H. Huang, F. Kang, Q.-H. Yang, Holey Graphitic Carbon Nitride Nanosheets with Carbon Vacancies for Highly Improved Photocatalytic Hydrogen Production, Adv. Funct. Mater., 25 (2015) 6885.

[38] Y. Cui, G. Zhang, Z. Lin, X. Wang, Condensed and low-defected graphitic carbon nitride with enhanced photocatalytic hydrogen evolution under visible light irradiation, Appl. Catal. B-Environ.,

181 (2016) 413.

[39] S. Li, G. Dong, R. Hailili, L. Yang, Y. Li, F. Wang, Y. Zeng, C. Wang, Effective photocatalytic H_2O_2 production under visible light irradiation at g-C_3N_4 modulated by carbon vacancies, Appl. Catal. B-Environ., 190 (2016) 26.

[40] S. Bai, N. Zhang, C. Gao, Y. Xiong, Defect engineering in photocatalytic materials, Nano Energy, 53 (2018) 296.

[41] P. Niu, M. Qiao, Y. Li, L. Huang, T. Zhai, Distinctive defects engineering in graphitic carbon nitride for greatly extended visible light photocatalytic hydrogen evolution, Nano Energy, 44 (2018) 73.

[42] Y. Zhang, S. Zong, C. Cheng, J. Shi, P. Guo, X. Guan, B. Luo, S. Shen, L. Guo, Rapid high-temperature treatment on graphitic carbon nitride for excellent photocatalytic H_2-evolution performance, Appl. Catal. B-Environ., 233 (2018) 80.

[43] Z. Hong, B. Shen, Y. Chen, B. Lin, B. Gao, Enhancement of photocatalytic H_2 evolution over nitrogen-deficient graphitic carbon nitride, J. Mater. Chem. A, 1 (2013) 11754.

[44] G. Liu, G. Zhao, W. Zhou, Y. Liu, H. Pang, H. Zhang, D. Hao, X. Meng, P. Li, T. Kako, J. Ye, In Situ Bond Modulation of Graphitic Carbon Nitride to Construct p-n Homojunctions for Enhanced Photocatalytic Hydrogen Production, Adv. Funct. Mater., 26 (2016) 6822.

[45] Z. Zhu, H. Pan, M. Murugananthan, J. Gong, Y. Zhang, Visible light-driven photocatalytically active g-C_3N_4 material for enhanced generation of H_2O_2, Appl. Catal. B-Environ., 232 (2018) 19.

[46] P. Niu, G. Liu, H.-M. Cheng, Nitrogen Vacancy-Promoted Photocatalytic Activity of Graphitic Carbon Nitride, J. Phys. Chem. C, 116 (2012) 11013.

[47] J. Wu, N. Li, H.-B. Fang, X. Li, Y.-Z. Zheng, X. Tao, Nitrogen vacancies modified graphitic carbon nitride: Scalable and one-step fabrication with efficient visible-light-driven hydrogen evolution, Chem. Eng. J., 358 (2019) 20.

[48] L. Luo, A. Zhang, M.J. Janik, K. Li, C. Song, X. Guo, Inorganic salt-assisted fabrication of graphitic carbon nitride with enhanced photocatalytic degradation of Rhodamine B, Mater. Lett., 188 (2017) 130.

[49] P. Hu, C. Chen, R. Zeng, J. Xiang, Y. Huang, D. Hou, Q. Li, Y. Huang, Facile synthesis of bimodal porous graphitic carbon nitride nanosheets as efficient photocatalysts for hydrogen evolution, Nano Energy, 50 (2018) 376.

[50] R. Godin, Y. Wang, M.A. Zwijnenburg, J. Tang, J.R. Durrant, Time-Resolved Spectroscopic Investigation of Charge Trapping in Carbon Nitrides Photocatalysts for Hydrogen Generation, J. Am. Chem. Soc., 139 (2017) 5216.

[51] Q. Ruan, T. Miao, H. Wang, J. Tang, Insight on Shallow Trap States-Introduced Photocathodic Performance in n-Type Polymer Photocatalysts, J. Am. Chem. Soc., 142 (2020) 2795.

[52] C. Merschjann, S. Tschierlei, T. Tyborski, K. Kailasam, S. Orthmann, D. Hollmann, T. Schedel-Niedrig, ArneThomas, S. Lochbrunner, Complementing Graphenes: 1D Interplanar Charge Transport in Polymeric Graphitic Carbon Nitrides, Adv. Mater., 27 (2015) 7993.

[53] L. Luo, A. Zhang, M.J. Janik, K. Li, C. Song, X. Guo, Facile fabrication of ordered mesoporous graphitic carbon nitride for RhB photocatalytic degradation, Appl. Surf. Sci., 396 (2017) 78.

[54] Z. Zeng, X. Quan, H. Yu, S. Chen, Y. Zhang, H. Zhao, S. Zhang, Carbon nitride with electron storage property: Enhanced exciton dissociation for high-efficient photocatalysis, Appl. Catal. B-Environ., 236 (2018) 99.

[55] G. Zhang, M. Zhang, X. Ye, X. Qiu, S. Lin, X. Wang, Iodine modified carbon nitride semiconductors as visible light photocatalysts for hydrogen evolution, Adv. Mater., 26 (2014) 805.

[56] L. Luo, A. Zhang, M.J. Janik, C. Song, X. Guo, Facile fabrication of metal-free urchin-like g-C_3N_4 with superior photocatalytic activity, RSC Adv., 6 (2016) 94496.

[57] V.R. Battula, S. Kumar, D.K. Chauhan, S. Samanta, K. Kailasam, A true oxygen-linked heptazine based polymer for efficient hydrogen evolution, Appl. Catal. B-Environ., 244 (2019) 313.

[58] S. Sun, W. Wang, D. Li, L. Zhang, D. Jiang, Solar Light Driven Pure Water Splitting on Quantum Sized BiVO4 without any Cocatalyst, ACS Catal., 4 (2014) 3498.

[59] Q. Xu, B. Cheng, J. Yu, G. Liu, Making co-condensed amorphous carbon/g-C_3N_4 composites with improved visible-light photocatalytic H_2 -production performance using Pt as cocatalyst, Carbon, 118 (2017) 241.